Catal Lett (2015) 145:420–435
DOI 10.1007/s10562-014-1437-8

Towards a Molecular Level Understanding of the Multi-Electron Catalysis of Water Oxidation on Metal Oxide Surfaces

Miao Zhang · Heinz Frei

Received: 17 October 2014 / Accepted: 13 November 2014 / Published online: 23 November 2014

Abstract Earth abundant metal oxides play a central role as catalysts in the essential chemical transformations of sunlight to fuel conversion, which are the oxidation of water and the reduction of carbon dioxide. The rapidly growing interest in renewable fuel generation by using the energy of the sun has recently led to substantial breakthroughs in the use of first row transition metal oxides as catalysts for oxygen evolution from water. Substantive improvements of rates and lowering of overpotentials have been achieved by exploiting materials properties on the nanoscale, or taking advantage of the synergy of multiple metals. Moreover, knowledge derived from mechanistic investigations with structure specific spectroscopy is accelerating efficiency improvements. Monitoring by time-resolved FT-infrared spectroscopy reveals the molecular nature of active sites, while in situ X-ray and optical spectroscopy under reaction conditions provides insights into the electronic structure of the surface metal centers participating in the catalysis. By combining the bond specificity of vibrational spectroscopy with the metal electronic structure specificity of optical, X-ray absorption or photoelectron spectroscopy, a complete understanding of active surface sites on metal oxides begins to emerge. Charge flow driving the chemical transformations probed by optical spectroscopy across time scales from ultrafast to very slow reveals the processes that control the productive use of charges delivered to the catalyst. Coupling of the water oxidation catalysis at a metal oxide catalyst with carbon dioxide reduction at a heterobinuclear chromophore, which is the goal of the artificial photosystem approach, is demonstrated by a well-defined all-inorganic polynuclear unit.

Keywords Heterogeneous catalysis · Photocatalysis · Water oxidation · Spectroscopy · Surface reaction kinetics · Oxide supports

1 Introduction

Metal oxides play a central role in two essential catalytic transformations for the generation of renewable fuels from abundant resources, which are the reduction of carbon dioxide and the oxidation of water. When coupled together, these two reactions constitute a sustainable cycle, since use of the resulting fuel in a fuel cell or by direct combustion regenerates the reactants CO_2 and H_2O. If powered by the sun, either in a single integrated system (artificial photosynthesis) or in a two-step configuration consisting of photon to electricity conversion by photovoltaics coupled to an electrolyzer, the cycle offers a path towards replacing fossil resources by renewable fuels. Realization of such a technology on a scale that will have an impact on global fuel consumption (terawatt scale) requires catalysts that are both robust and Earth abundant, properties shared by a variety of metal oxides. In the past several years, substantial breakthroughs have been made in engaging abundant metal oxides as efficient catalysts for water oxidation. Promising developments in metal/metal oxide based catalysis of carbon dioxide reduction are emerging as well. Nevertheless, catalysts for converting carbon dioxide to a fuel, especially a liquid transportation fuel with adequate activity operating at acceptable overpotential are a formidable challenge that has yet to be met.

M. Zhang · H. Frei (✉)
Lawrence Berkeley National Laboratory, Physical Biosciences Division, University of California, Berkeley, CA 94720, USA
e-mail: HMFrei@lbl.gov

In the area of catalysts for water oxidation, recent efficiency improvements have been particularly impressive for first-row transition metal oxides. Taking early studies of electro- or photon-driven Co and Mn oxide catalysts as point of departure [1–16], development of nanostructured forms of these oxides featuring very high surface areas have dramatically increased turnover frequencies of O_2 product formation per projected catalyst area [17–19]. The need for high turnover frequency per projected area in artificial photosynthesis is based on the requirement that the catalyst should keep up with the incident solar flux in order to minimize wasting of photons. Furthermore, controlled substitution of Co or Mn by a second metal such as Ca or Li, partly inspired by the Mn_4O_4Ca catalyst complex of the natural photosystem (PS II) [20], was found to result in marked rate enhancements compared to monometallic oxides [21–24].

Understanding of reaction mechanisms at the liquid–solid or gas–solid catalyst interface is the key for guiding catalyst design and choice of reaction conditions for boosting efficiency. High efficiency in the context of solar light driven catalysis means conversion of a maximum fraction of the photon energy to chemical energy of the fuel, which requires that the catalyst operates close to the thermodynamic potential of water oxidation. Equally important, the majority of incident photons need to be utilized productively for the chemical transformation of water and carbon dioxide, especially at maximum solar intensity. Particularly helpful is the direct observation of surface chemical functionalities by structure specific spectroscopies under reaction conditions. If conducted with sufficient temporal resolution for capturing short lived intermediates and monitoring their kinetic behavior, knowledge can be gained about the kinetic relevancy and the role of a given surface species in the catalytic cycle.

In this article, we will focus on recent advances in the understanding of elementary catalytic steps of water oxidation on metal oxides based on monitoring by time-resolved FT-IR, steady state Raman, X-ray absorption and emission, X-ray photoelectron and transient optical spectroscopy under reaction conditions. From such studies, molecular level knowledge of surface intermediates is emerging that allows comparison with analogous transformations of homogeneous transition metal catalysts, deepening our mechanistic insights. Knowledge of the geometrical and electronic structure of the metal oxide catalyst material and its surface is very important for the understanding of structural motifs available for catalytic transformations to take place, and of pathways for the transport of charges from the location of injection to the catalytic sites. The new level of detailed understanding of catalytic mechanisms established by recent studies provides concrete guidance for improved designs of metal oxide catalysts. While primarily focusing on water oxidation, the article includes a discussion of a well-defined polynuclear oxide unit that accomplishes the direct coupling of the water oxidation chemistry with carbon dioxide reduction, thereby closing the photosynthetic cycle.

2 Cobalt Oxide Water Oxidation Catalysts

In the past several years, exploration of cobalt oxides as water oxidation catalysts has resulted in very substantial advances in terms of efficiency of this oxide material and the understanding of surface chemical functionalities responsible for the activity.

2.1 High Turnover Frequency Through Nanostructuring

Exploring the possibility of a several orders of magnitude increase of the number of Co surface centers of a Co_3O_4 particle through nanostructuring while at the same time providing a robust scaffold for a stable dispersion of the clusters, we developed crystalline Co_3O_4 nanorod bundles in mesoporous silica SBA-15. This mesoporous silica material consists of uni-dimensional channels of 8 nm diameter separated by walls of 2 nm thickness with interconnecting micropores. The synthesis consisted of wet impregnation of Co nitrate precursor followed by calcination at 550 C [17, 18], resulting in the formation of spheroid-shaped Co oxide nanoclusters shown in the TEM image of Fig. 1a (4 wt% Co loading). Removal of the silica scaffold by etching reveals a nanorod bundle structure of the Co oxide cluster with the rods interconnected by small bridges, confirming that the catalyst is a replica of the SBA-15 pore structure (Fig. 1c, d). The atomic structure of the Co oxide clusters is crystalline Co_3O_4 (spinel) for both the 4 and 8 wt% sample, as shown by the XRD pattern [17] and most clearly evidenced by extended X-ray fine structure (EXAFS) data presented in Fig. 1b.

These high surface area clusters exhibit turnover frequencies (TOF) per projected area for O_2 evolution from water under mild conditions (pH 6) at room temperature that exceed by far those of unstructured Co_3O_4, micrometer sized crystals. The activity of the Co_3O_4 clusters in aqueous suspension was measured by driving the catalyst with a visible light sensitizer using the established light absorber $[Ru(bpy)_3]^{2+}$ (bpy = 2,2′-bipyridine) in conjunction with $S_2O_8^{2-}$ as electron acceptor [16, 25]. The method involves excitation of the Ru complex by visible light (476 nm), resulting in instant oxidation to $[Ru(bpy)_3]^{3+}$, a moderate oxidant ($\varepsilon^0 = 1.24$ V NHE) upon electron transfer to persulfate. When encountering a Co_3O_4 cluster inside the SBA-15 channels, holes are sequentially transferred to

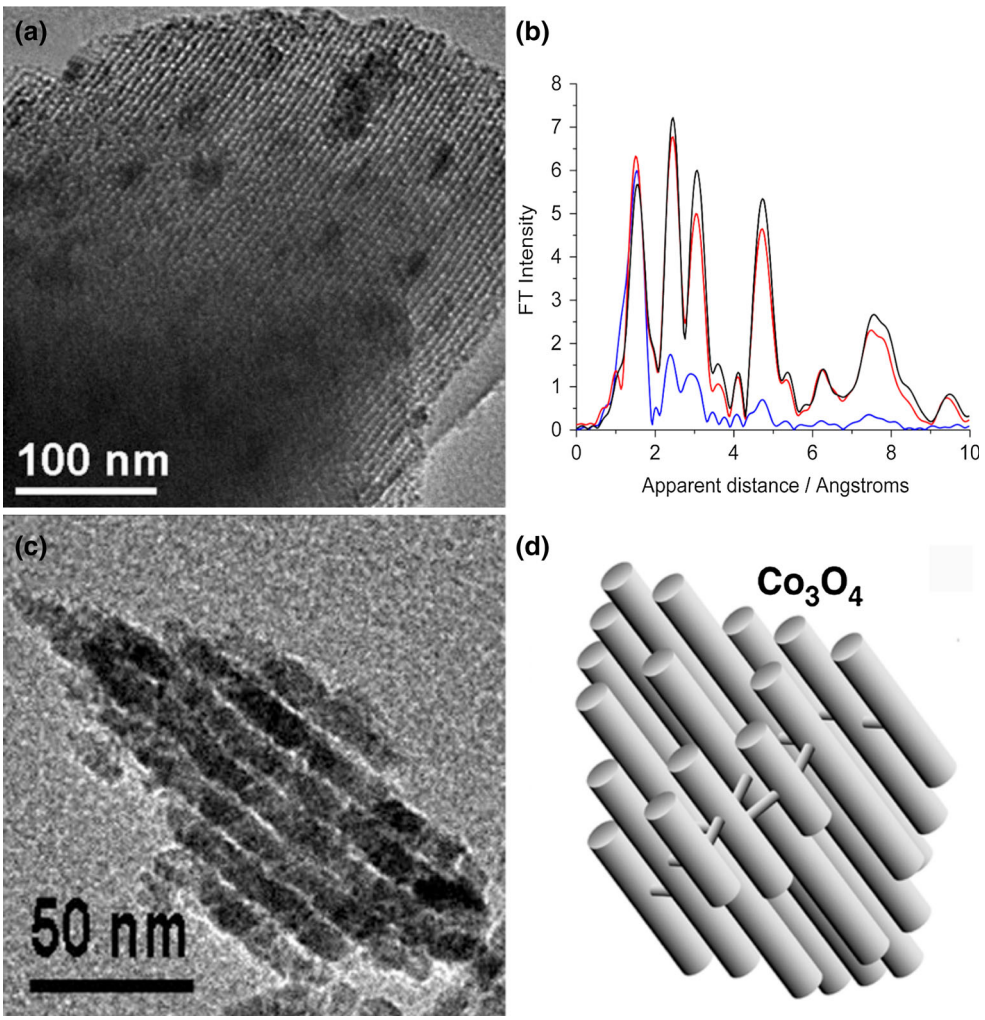

Fig. 1 Co_3O_4 nanocluster catalyst supported on mesoporous silica SBA-15. **a** TEM image of SBA-15 loaded with Co_3O_4 nanorod bundle (4 wt%). **b** Co EXAFS data of reference). The lower FT-EXAFS peak intensity for higher shells of the 4 % sample is due to the small size of the particles. **c** Bare Co_3O_4 nanocluster after removal of the SBA-15 silica material using aqueous NaOH as etching agent. **d** Cartoon of catalyst structure. From Ref. 17, with permission

Co_3O_4 [17]. This sensitizer system is a convenient surrogate for catalyst activity evaluation and mechanistic studies, and is replaced by all-inorganic heterobinuclear light absorbers in artificial photosystems as described in Sect. 6. By measuring mass spectrometrically the O_2 gas buildup in the head space of an aqueous suspension of SBA-15 particles loaded with Co_3O_4 nanoclusters (abbrev. SBA-15/Co_3O_4) upon visible light sensitization, the O_2 growth shown in Fig. 2 was obtained. From the linear rise of O_2 over the initial 30 min of photolysis for the SBA-15/Co_3O_4 (4 %) catalyst (Fig. 2, trace d) and the total number of clusters suspended in the solution, a TOF of 1,140 O_2 molecules s^{-1} per Co_3O_4 nanocluster was calculated (the levelling off of the O_2 buildup around 60 min of photolysis is due to depletion of persulfate acceptor. Replenishing the solution with acceptor resulted in continued water oxidation at the original rate, indicating undiminished activity of the catalyst) [17, 18]. The projection of the 35 nm diameter

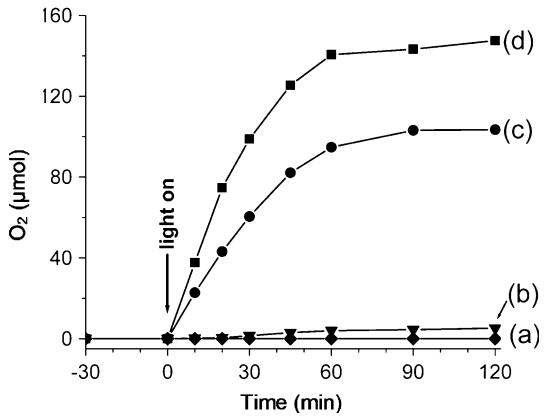

Fig. 2 Oxygen evolution in aqueous suspensions recorded by mass spectroscopy of **a** SBA-15/NiO (8 %) serving as catalytically inactive control. **b** Micrometer sized Co_3O_4 particles. **c** SBA-15/Co_3O_4 (8 %). **d** SBA-15/Co_3O_4 (4 %). Measurements were conducted at pH 5.8 and 22 °C. From Ref. 17, with permission

spheroidal cluster on a plane perpendicular to the solar beam is 1,000 nm^2, which gives a TOF per projected area of the catalyst around one O_2 molecule s^{-1} nm^{-2}. A rate of 100 O_2 s^{-1} nm^{-2} is sufficient for keeping up with the photon flux at maximum solar intensity (at noon in summer) [18]. Therefore, stacking of an average of 100 Co_3O_4 clusters, which can readily be achieved by pressing a powder of SBA-15/Co_3O_4 particles into a thin wafer (150 μm thickness for 4 % loading) provides a catalyst sample for water oxidation that is both kinetically and thermodynamically competent (the overpotential is a moderate 350 mV (1.24–0.89 V, $\varepsilon^0(O_2/H_2O) = 0.89$ V NHE at pH 5.8).

Comparison of the water oxidation activity of the SBA-15 supported Co_3O_4 nanostructured clusters with the activity of micron size Co_3O_4 particles (Fig. 2, trace b), normalized to equal weight, reveals a 1,550 times higher O_2 evolution rate for the 35 nm nanorod bundle catalyst. The principal factor for the several orders of magnitude higher rate of the nanostructured Co_3O_4 is the nearly 100 times greater number of surface Co centers per geometrical oxide surface area. We attribute the additional factor of 16 larger TOF value for the nanorod bundle catalyst to the correspondingly higher activity of its surface Co centers compared to those of the μm sized particle. The enhanced activity could be due to a higher density of surface motifs with adjacent $Co^{III}OH$ groups ($Co^{III}(OH)$–O–$Co^{III}OH$) in the case of nanorod bundles in silica, which were recently identified as highly active catalytic sites (Sect. 2.2). Assuming that all surface Co centers of the crystalline Co_3O_4 nanorod bundle are catalytically active, we calculate an average TOF per surface Co center of of 0.01 O_2 s^{-1} [17]. These findings have recently been confirmed and expanded by work from other laboratories. For example, a comparison of the water oxidation activity of surfactant-free 3 nm Co_3O_4 particles in aqueous pH 6 solution with the same nanoparticles supported on SBA-15 using the same visible light sensitization method, Grzelczak et al. confirmed the significantly improved yields for the SBA-15 supported particles because of the prevention of particle aggregation [26]. Jiao and his colleague reported the higher activity Co_3O_4 nanoparticles inside SBA-15 as well. Interestingly, the same Co_3O_4 nanoparticle catalysts in mesoporous silica KIT-6 with its 3-dimensional network of 8 nm channels perform even better than in SBA-15, presumably because of more facile diffusion of sensitizer and reactants in this more accessible channel system [27].

TOF values were subsequently reported for electrocatalytically driven cubical Co_3O_4 nanoparticles (range 5–50 nm) under basic (pH 14) conditions. For these measurements, the Co oxide crystals were supported by a Ni foam anode [28]. According the electrochemical measurements the TOF per nanoparticle increases linearly with the accessible surface area of the particle. This finding supports the conclusion that the catalytic activity is proportional to the number of exposed Co centers. The tenfold higher TOF = 0.12 O_2 s^{-1} per surface Co center at pH 14 [28] compared to 0.01 at pH 6 is in agreement with the more facile oxidation of hydroxide ion compared to H_2O under neutral or acidic conditions. The catalytic yield dependence on the surface area of Co_3O_4 nanoparticles in this same size range was recently confirmed under visible light sensitized and close to neutral pH conditions [26]. In our most recent studies of surfactant-free Co_3O_4 nanocrystals (5 nm diameter) or Co_3O_4 nanotubes in aqueous suspensions at pH 7–8, measurement of water oxidation activity with the $Ru(bpy)_3$ visible light sensitizer approach revealed TOF values per surface Co center between 0.01 and 0.02 O_2 s^{-1} [29–31]. Hence, nanostructured crystalline Co_3O_4 proves to be a suitable catalytic material for water oxidation in a variety of morphological forms, which provides flexibility in developing various architectures for integrating the water oxidation catalyst into complete synthetic solar fuel conversion systems.

2.2 Molecular Nature of Active Surface Sites Revealed by Transient FT-IR Spectroscopy

While the observed activity of surface Co centers is in the proper range for designing catalyst morphologies that are able to keep up with the solar flux, further improvement of the rate to broaden the range of particle sizes and morphologies requires detailed knowledge of the active sites. Specifically, do most surface Co sites operate at TOF of 0.01–0.02 s^{-1}, or are there sites running at much higher TOF while other surface Co centers barely contribute or even play the role of spectators? If so, what is the nature of the most active site? Knowledge of the structural motif of the most active site(s) and understanding of the elementary reaction steps is the key for guiding modifications of Co oxide surfaces for maximizing the TOF.

To answer these questions, we have conducted a mechanistic study of water oxidation on Co_3O_4 surfaces by time-resolved rapid-scan FT-IR spectroscopy using crystalline nanoparticles in aqueous solution [32]. A TEM image of the catalyst particles at 1 A resolution is shown in Fig. 3a [33]. The visible light sensitization method using the $[Ru(bpy)_3]^{2+}$—persulfate system provided a straightforward means of pulsed charge (hole) delivery to the Co_3O_4 catalyst particles, which is required for obtaining temporally resolved spectra. An aqueous suspension of the surfactant-free Co_3O_4 nanoparticles held at pH 8 was placed on an attenuated total reflection (ATR) element (3 reflection diamond plate, Fig. 3b). Upon illumination of the solution with a visible laser pulse (476 nm) of 300 ms duration to excite the sensitizer, two infrared bands were

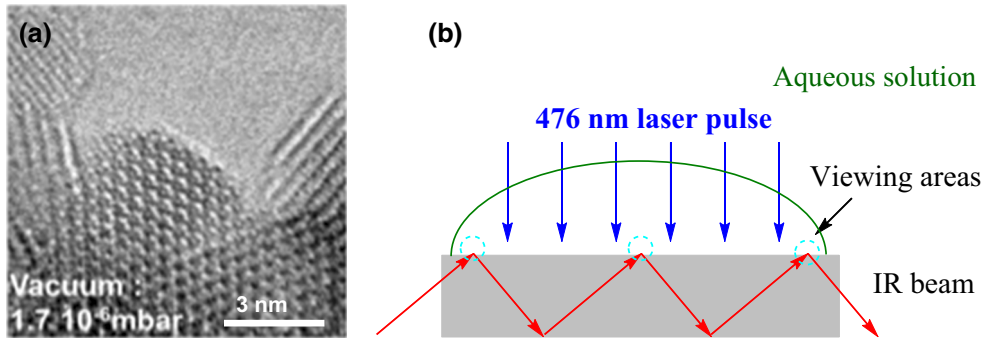

Fig. 3 **a** Atomic resolution TEM image of 5 nm Co_3O_4 crystallite. **b** Sample configuration for rapid-scan ATR FT-IR spectroscopy. A visible laser pulse (476 nm, 300 ms) excites the $Ru(bpy)_3$ sensitizer in an aqueous suspension of Co_3O_4 nanocrystals placed on a diamond ATR element with 3 infrared reflections. Image a is from Ref. 33, with permission

detected that exhibit very different kinetic behavior. One species absorbs at 1,013 cm^{-1} (Fig. 4Aa) and shows ^{18}O isotopic counterparts in pure $H_2^{18}O$ at 995 and 966 cm^{-1} (Fig. 4Ab). The large, 47 cm^{-1} isotope shift of the 966 cm^{-1} band reveals an OO bond mode, while the 1,013 cm^{-1} frequency indicates a superoxide structure that interacts with two Co centers [32, 34]. A modest D isotope shift of 38 cm^{-1} in D_2O to lower frequencies (band at 975 cm^{-1}, Fig. 4Ac) signals hydrogen bonding interaction of the superoxide moiety, most likely with an adjacent CoOH (CoOD) group. As shown in Fig. 4D, this 3-electron oxidation intermediate, which is just one charge transfer step short of liberating O_2, grows mostly during the 300 ms light pulse and as long as oxidized sensitizer species persist, but barely changes intensity afterwards. Evidently, arrival of another charge (hole) by continued illumination is required for the elimination of O_2 and restart of the catalytic cycle, as illustrated in the proposed catalytic scheme of Fig. 5. At the same time, electrochemical measurements with an O_2-sensitive Clark electrode indicate evolution of O_2 in response to such a 300 ms light pulse. Mass spectroscopic analysis of the gas accumulated in the head space of the reaction vessel when using pure $H_2^{18}O$ showed a ratio of $^{18}O_2$ to $^{18}O^{16}O$ of 8:1, with no unlabeled $^{16}O_2$ detected (Fig. 4C). The isotopic composition of the final O_2 product agreed with the composition of the superoxide intermediate after a mere 1,500 ms illumination (Fig. 4Ab, inset), which confirms that the surface superoxide species is a kinetically competent intermediate of the O_2 evolving catalytic cycle. Moreover, the complete absence of unlabeled superoxide and $^{16}O_2$ gas product in the $H_2^{18}O$ experiment indicates that the OO bond forming step involves attack by a water molecule from solution rather than direct coupling of two surface O of Co_3O_4 particles, a mechanistic question of much current interest in the field of water oxidation catalysis.

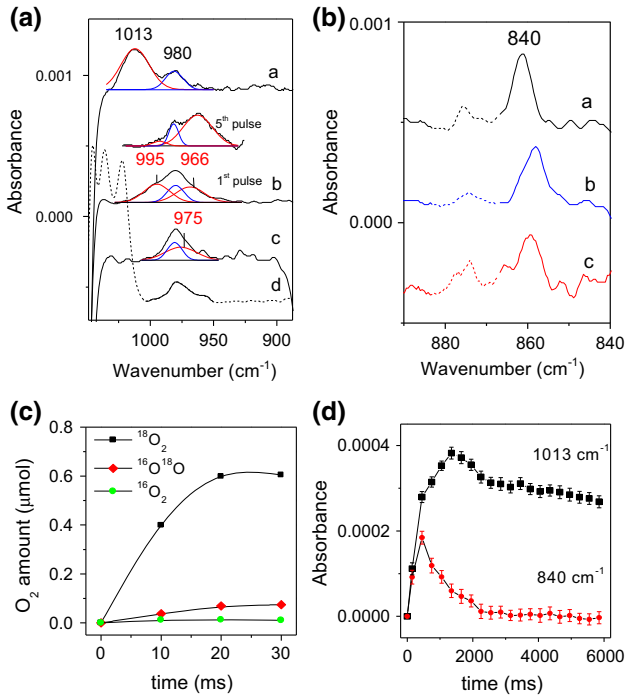

Fig. 4 Time resolved FT-IR monitoring of water oxidation catalysis at Co_3O_4 nanoparticles. **a** FT-IR of superoxide intermediate Co^{III}–(OO)–Co^{III} at 5,850 nm after onset of a 300 ms photolysis laser pulse *a* in $H_2^{16}O$, *b* $H_2^{18}O$ (*inset* spectral trace after 5 laser pulses), *c* D_2O, *d* control experiment, no Co_3O_4 present. *Red* superoxide bands, *blue* SO_4^{2-} growth (reduced acceptor). **b** Co^{IV}=O intermediate in *a* $H_2^{16}O$, *b* $H_2^{18}O$, *c* D_2O. **c** Isotopic composition of O_2 gas accumulated in headspace of $H_2^{18}O$ solution measured by mass spectroscopy. **d** Temporal behavior of superoxide (*black*) and Co^{IV}=O intermediate (*red*). From Ref. 32, with permission

A second intermediate was detected at 840 cm^{-1}, which does not exhibit an ^{18}O or D isotope shift. In contrast to the superoxide intermediate, the 840 cm^{-1} species decays spontaneously with a time constant of 1 s (Fig. 4B, D). The band is attributed to a Co^{IV}=O intermediate formed by oxidation of an octahedral $Co^{III}OH$ surface site in the first electron transfer step [32]. The spontaneous decay is assigned to O–O chemical bond formation upon

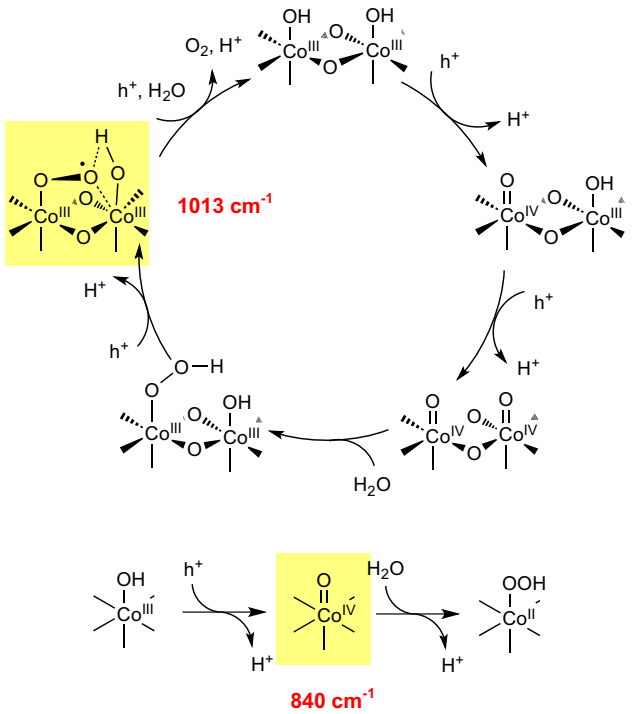

Fig. 5 Proposed catalytic mechanism of water oxidation on Co_3O_4 surface. *Top* Fast Co_3O_4 surface site. *Bottom* Slow Co_3O_4 surface site. The OO bond-forming step with H_2O in the fast cycle features the cooperative effect of adjacent electronically coupled Co^{IV}=O sites, which is absent in the H_2O addition reaction at the slow site. From Ref. 32, with permission

nucleophilic attack of H_2O to yield $Co^{II}OOH$ hydroperoxide intermediate (Fig. 5). Because the reaction time of 1 s is much slower than the rise of the superoxide intermediate (Fig. 4D), the 840 cm^{-1} Co^{IV}=O site cannot be a precursor of the observed superoxide. Rather, the 840 cm^{-1} surface species belongs to a much slower catalytic site of O_2 generation. While Co^{IV}=O has not been detected by vibrational spectroscopy before, Nocera and Britt have reported observation of the functionality by ex situ EPR measurement after electrochemical water oxidation at a Co oxide catalyst obtained by electrodeposition from a Co phosphate solution (Sect. 2.3) [35].

To identify the structural differences between the fast site that generates a superoxide intermediate and releases O_2 within 300 ms of driving the Co_3O_4 catalyst by visible light sensitization, and the slow site that advances merely to the Co^{IV}=O state and then reacts with H_2O, the various crystal surfaces of Co_3O_4 and insights from Pourbaix analyses of Co oxides reported in the literature were considered. Pourbaix analysis of electrodeposits of Co oxide showed that the most active structural phase, formed at applied electrochemical potentials sufficient for O_2 evolution from water, is a layered double hydroxide [36]. The prevalent motif of this structure consists of adjacent octahedral Co centers each with an OH group, linked by oxo bridges [36]. Because all crystallographic facets of Co_3O_4 have octahedrally coordinated Co^{III} centers linked by an oxo bridge [37], OH terminated surfaces feature many sites with this same Co^{III}(OH)–O–Co^{III}OH motif. Therefore, we propose that the fast catalytic site consists of two adjacent octahedral Co^{III} centers coupled by an oxo bridge, each with an OH ligand. Following oxidation of the two Co^{III}OH centers to adjacent Co^{IV}=O sites by two sequential holes, nucleophilic attack of a water molecule produces a CoOOH (hydroperoxide) functionality under reduction of both Co centers to Co^{III} in a spin allowed, near-geometry conserving process (Fig. 5, top). Oxidation by a subsequent hole generates the observed superoxide surface intermediate, and yet another hole expels O_2 and restarts the cycle. Hence, the TOF of the fast site is at least 3 s^{-1}, which is over 150 times faster than the estimated average rate per surface Co. On the other hand, the slow site (840 cm^{-1} band) is proposed to originate from oxidation of an octahedral Co^{III}OH group that is not linked to another Co^{III}OH site, leading to an isolated Co^{IV}=O instead (Fig. 5, bottom). Without the additional driving force imparted by an electronically coupled second Co^{IV}=O and a spin flip imposed by reduction to Co^{II}, a much slower O–O bond forming step is expected, as observed.

These molecularly defined surface intermediates, observed here for the first time for water oxidation by an Earth abundant metal oxide catalyst under reaction conditions, provide the knowledge needed for modifying catalysts to enhance efficiency. Specifically, ideas can now be developed for increasing the density of octahedrally coordinated Co^{III}(OH)–O–Co^{III}OH sites on Co oxide surfaces, which at this point has emerged as the most critical factor for accelerating the catalytic cycle.

2.3 Electronic Structure of Metal Surface Centers Monitored by X-ray Spectroscopy

The central role of oxo-bridged octahedral Co(OH)–O–CoOH sites in the widely studied Co oxide electrodeposits from Co^{2+} solutions in phosphate electrolyte introduced by Nocera and his colleague [38] was recognized by combined electrokinetic and cyclic voltammetry studies. Specifically, a fast, one-electron, one-proton equilibrium which precedes the O–O bond forming reaction is attributed to $Co^{III}(OH)-O-Co^{IV}=O \rightarrow Co^{IV}(=O)-O-Co^{IV}=O$ conversion [39]. Ex situ electron paramagnetic resonance spectroscopy (EPR) of these electrocatalytic films after reaction showed the buildup of Co^{IV}=O sites by a $g_{eff} = 2.27$ signal characteristic for $Co^{IV}(S = 1/2)$ (Fig. 6a) [35]. Moreover, a shift towards higher energy of the X-ray absorption near edge structure (XANES) of the

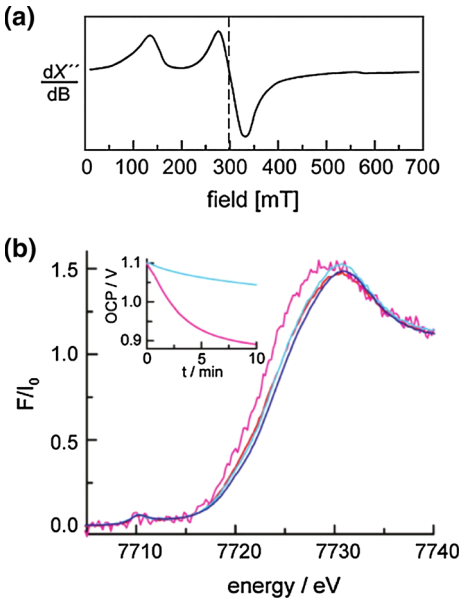

Fig. 6 Spectroscopy of electrodeposited Co oxide catalytic film. **a** Ex situ EPR spectrum (4 K) of a Co oxide film that was exposed to an applied potential of 1.34 V showing the Co^{IV} signal. From Ref. 35, with permission. **b** XANES spectra of Co oxide film recorded in situ during electrocatalytic water oxidation showing surface at open circuit potential (*magenta*) and 1.25 V (*red*). As reference, bulk Co oxide film at open circuit potential (*cyan*) and 1.25 V (*blue*) are shown. From Ref. 40, with permission

Co K-edge was observed during electrocatalytic water oxidation, indicating that the oxidation state of some fraction of Co centers rises to IV under steady state conditions (Fig. 6b) [40]. These EPR and X-ray spectroscopic signals report on the electronic state of the metal center, thereby complementing the chemical bond information during the catalytic cycle that can be obtained by temporally resolved FT-IR spectroscopy. Future time resolved (pulsed) EPR and transient X-ray spectroscopy studies on such systems will likely provide new mechanistic insights about the precise electronic structure of the metal centers at each step of the catalytic cycle. This is particularly important in light of possible extensive charge delocalization across multiple Co centers as suggested by recent multi-frequency EPR studies of a $Co_4(III^3,IV)O_4$ oxo-bridged Co cubane model compound [41]. For understanding the dynamics of the wider domain structure of Co oxide electrodeposits under catalytic conditions which may influence reaction pathways, pair distribution function analysis of X-ray scattering probes longer range distances not accessible by EXAFS spectroscopy. The recent finding by Tiede based a study of an amorphous Co oxide electrocatalyst that distorted coordination geometries may contribute to catalytic activity demonstrates the important role of this technique [42, 43].

While no transient surface intermediates of (dark) electrochemically driven water oxidation on Co oxide films have been reported, structural phase transformations have been uncovered in the case of Co_3O_4 when tuning the applied potential towards levels needed for initiating catalysis. It is known from Pourbaix analysis that at an applied potential of +0.75 V (NHE, pH 7) the Co_3O_4 spinel phase transforms reversibly to the Co oxy hydroxide phase (Co(O)OH) [44]. In situ Raman [45] and X-ray spectroscopy [46] afford direct monitoring of the structural change, with results in agreement with theory [47, 48]. Knowledge of the structural phase of the oxide catalyst at the onset of catalytic activity is an important step towards learning about the detailed mechanism.

2.4 Molecular Metal Oxide Analogues Contributing to Mechanistic Understanding

Mechanistic comparisons of solid metal oxide catalysts with molecular polynuclear metal oxo analogues, where available, provide valuable insights. Molecular catalysts for water oxidation range from all-inorganic polyoxometalate clusters featuring a Co oxide core $\left[Co_4(H_2O)_2(PW_9O_{34})_2\right]^{10-}$ [49] to a variety of organometallic complexes involving late transition metals. Spectroscopic observations that provide interesting comparisons with the Co_3O_4 catalyst are available in particular for Ru based O_2 evolving catalysts. For example, in the case of the extensively studied water oxidation catalyst *cis,cis*-$[(bpy)_2(H_2O)Ru^{III}ORu^{III}(H_2O)(bpy)_2]^{4+}$ with a Ru–O–Ru core ('blue dimer'), a $Ru^{V}(=O)ORu^{V}(=O)$ intermediate was found to undergo O–O bond formation by nucleophilic attack of H_2O to yield a hydroperoxide intermediate

$$Ru^{V}(=O)ORu^{V}(=O) + H_2O \rightarrow Ru^{IV}(OH)ORu^{IV}OOH \rightarrow Ru^{V}(=O)ORu^{III}OOH + H^{+} \quad (1)$$

Both protonated and deprotonated form of the intermediate are directly observed by pairs of optical absorptions at 451, 750 nm and 482, 850 nm, respectively [50, 51]. This hydroperoxide forming step (1) is analogous to the O–O bond forming step $Co^{IV}(=O)OCo^{IV}=O \rightarrow Co^{III}(OH)OCo^{III}OOH$ proposed for the Co_3O_4 catalyst and demonstrates the accelerating effect of adjacent, electronically coupled high valence oxo centers for O–O bond formation. Single center Ru molecular catalysts are capable of evolving O_2 evolution from water as well [52, 53]. Optical and resonance Raman spectra of water oxidation intermediates of a mononuclear Ru polypyridyl complex obtained by electrochemical, stopped-flow and nanosecond pulse radiolysis experiments gave structural and kinetic insights on intermediates supported by theory that provided an early precedent for a single high valent metal oxo attacking H_2O to form an O–O bond [54]. Very recently, a mononuclear organo Co complex was shown to oxidize water by forming the

O–O bond by nucleophilic attack of H_2O on a Co^{IV}–OH moiety [55], closely reflecting the proposed mechanism for single Co^{IV}=O sites on the Co_3O_4 surface (Fig. 5).

3 Mn Oxide Water Oxidation Catalysts

Manganese oxides have received particular attention as catalysts for water oxidation for a long time, in part because of the unique role of this oxide in the natural photosystem in the form of the $CaMn_4O_4$ cluster [20].

3.1 Nanostructuring for High Turnover Frequency

Similar to the case of Co oxides, there is a history of the use of Mn oxides as anode coatings for electrocatalytic water oxidation, typically under high pH conditions [13]. Yet the early reports suggested that Mn oxides hold promise for sufficiently fast water oxidation catalysts under mild pH conditions as well if nano-sized clusters with high surface area can be made. Using the same approach as in the case of Co_3O_4 of substantially increasing the number of metal surface centers of Mn oxide particles by nanostructuring, we explored crystalline Mn oxide nanostructured clusters in mesoporous silica scaffolds [18, 19]. Synthesis of highly nanostructured Mn oxide clusters of spherical shape in silica material of type KIT-6 with its 3-dimensional network of 8 nm diameter channels gave efficient water oxidation catalysts under close to neutral pH conditions. Figure 7a shows a TEM image of nanostructured Mn oxide clusters inside a KIT-6 scaffold (8 %wt loading). The clusters of 80 nm diameter with narrow size distribution replicate the internal KIT-6 mesopore support structure, which remains intact even after calcination at high temperature. Mn K-edge X-ray absorption spectroscopy provided detailed information on the atomic structure of the clusters, exploiting the fact that the K-edge position depends linearly on the Mn oxidation state (shift to higher energy with increasing oxidation state). As shown in Fig. 7b, the average oxidation state varies with calcination temperature, which allowed us to determine the structural composition that gave the highest catalytic activity. A component analysis study of the XANES signal based on reference spectra of β-MnO_2, α-Mn_2O_3, and Mn_3O_4 revealed the fractional composition of the mixed-phase catalyst for each calcination temperature [19].

The cluster with the highest water oxidation activity as measured by the visible light sensitization method ($[Ru(bpy)_3]^{2+} - S_2O_8^{2-}$ system) discussed above (Sect. 2.1) showed TOF = 3,330 O_2 s^{-1} and consists of Mn_2O_3 as the dominant phase (80 %), with MnO_2 (14 %) and Mn_3O_4 (6 %) as minor phases. No degradation of activity or structural integrity of the Mn oxide nanoclusters was noted upon several hours of O_2 evolution according to the XANES spectra and ICP analysis of the solution after photolysis, indicating reasonable stability under mild pH conditions. Taking into account the geometrical area of the Mn oxide nanocluster projected on a plane, we calculate TOF = 0.6 s^{-1} nm^{-2} projected area, not far from the 1 s^{-1} nm^{-2} value for Co_3O_4 nanocluster catalysts. Therefore, the nanostructured Mn oxide clusters supported by the KIT-6 mesoporous silica constitute an environmentally friendly, stable inorganic catalyst operating under mild aqueous conditions and modest overpotential (350 mV). The silica environment may play an important role in preventing the surface of the metal oxide catalyst from restructuring, in addition to providing a stable dispersion that prevents agglomeration of the catalyst particles over time. The large effect of surface area enlargement by nanostructuring on the water oxidation efficiency was recently confirmed by a direct comparison of various Mn oxide morphologies in the absence of a supporting silica scaffold [56].

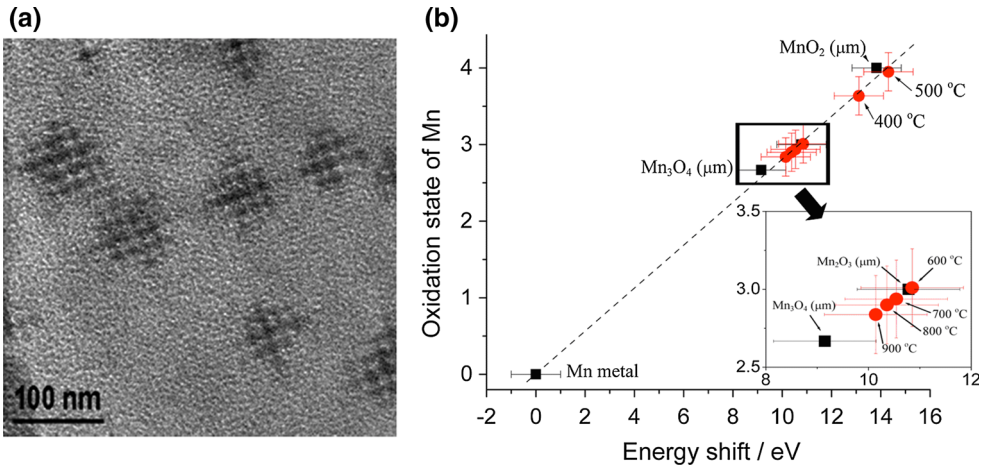

Fig. 7 Nanostructured Mn oxide cluster catalyst inside mesoporous silica KIT-6. **a** TEM image of cluster prepared by calcination at 800 °C. **b** Average oxidation state of Mn for Mn oxide nanoclusters prepared at different calcination temperature, derived from K-edge energies. From Ref. 19, with permission

3.2 Mn Electronic State Monitored In Situ by Optical and X-ray Spectroscopy

Optical monitoring of water oxidation catalysis at MnO_2 nanoparticles driven electrochemically has recently provided the first observation of intermediate species formed on the catalyst surface [57]. As shown in Fig. 8, an optical absorption band with a maximum at 510 nm is detected by diffuse transmission spectroscopy at the aqueous-solid interface of a δ-MnO_2 nanoparticle film attached to a transparent oxide anode (fluorine doped tin oxide, FTO) at potentials of 1.2 V SHE and higher. At this threshold potential, O_2 evolution is observed. The band is assigned to the d–d transition of Mn^{3+} centers, which was corroborated by the use of a chemical probe [57]. However, the chemical functionality of the surface site associated with the Mn^{3+} signal awaits identification by a structure specific spectroscopy, which will be required for determining the role of the intermediate in the catalytic water oxidation cycle.

For another type of Mn oxide catalyst electrodeposited on a Au/Ti electrode suitable for in situ X-ray absorption spectroscopy (XANES and EXAFS) under electrocatalytic conditions, Jaramillo and coworkers have identified distinct structural phases present under water oxidation and oxygen reduction conditions for one and the same electrodeposit [58, 59]. The XANES spectrum of the Mn oxide catalyst film measured under O_2 reduction conditions (0.7 V RHE, pH 13), shown in Fig. 9a agrees well with that of a Mn_3O_4 reference sample whose structure is depicted in Fig. 10a. The shift of the K-edge to lower energy, Fig. 9a, signals reduction of the metal to Mn^{II} with the observed edge energy closely matching the valence of 2.7 for Mn_3O_4. The structural assignment is further supported by comparison of Mn K-edge EXAFS measurements for the catalyst under O_2 evolution conditions with Mn_3O_4 EXAFS data,

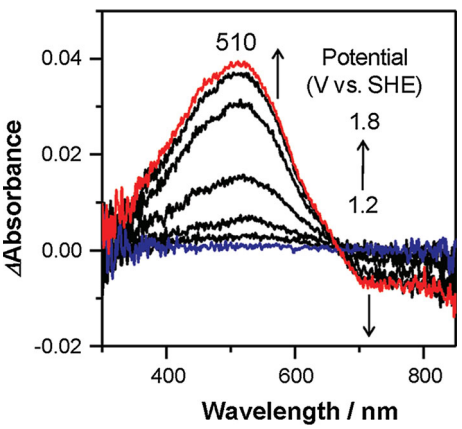

Fig. 8 Diffuse transmission optical absorption spectroscopy of Mn oxide nanoparticles under electrocatalytic conditions. Changes of the δ-MnO_2 film with increasing potential in the range 1.2–1.8 V SHE are shown. Spectra at 1.2 and 1.8 V are colored *blue* and *red*, respectively. From Ref. 57, with permission

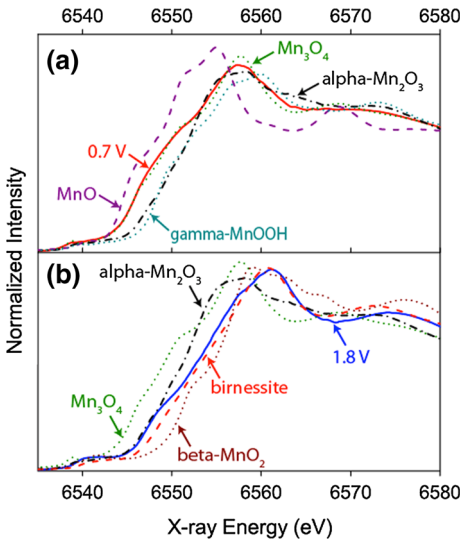

Fig. 9 XANES spectroscopy of Mn oxide catalytic film deposited on Au/Ti-electrode under reaction conditions. **a** MnO_x/Au-Si_3N_4 film poised at 0.7 V overlaid with reference materials MnO, Mn_3O_4, α-Mn_2O_3, and γ-Mn(O)OH. **b** MnO_x/Au-Si_3N_4 film poised at 1.8 V overlaid with reference materials Mn_3O_4, α-Mn_2O_3, birnessite, and β-MnO_2. From Ref. 58, with permission

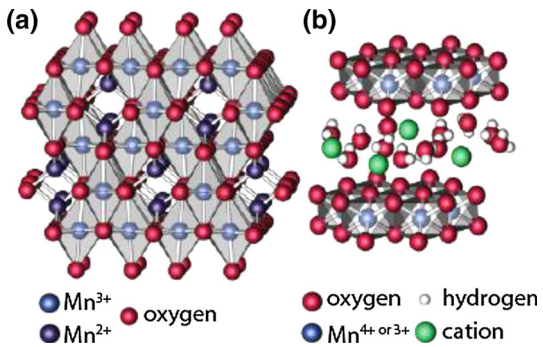

Fig. 10 Schematic showing crystal structures of **a** Mn_3O_4 consisting of octahedral (*light blue*) and tetragonal (*dark blue*) Mn sites. **b** Birnessite structure consisting of sheets of edge-sharing MnO_6 octahedra with cations and water intercalated into the interlayer space. From Ref. 58, with permission

although the amplitudes of the sample are considerably lower due to polycrystallinity with small domain sizes of the electrodeposit (Fig. 11a). In contrast, the XANES profile of the same MnO_x electrodeposit under water oxidation conditions (1.8 V RHE, pH 13) shifts to higher energy and is similar to the α-Mn_2O_3 phase (Fig. 9b). The profile most closely agrees with that of H^+ and Mg^{2+} birnessite phases with a layered structure and an average Mn oxidation state of 3.7 whose cartoon structure is shown in Fig. 10b. More accurately, composition analysis indicates birnessite (80 %) and Mn_3O_4 (20 %) [58]. Agreement of the EXAFS traces of Mg^+ birnessite and the catalyst under O_2 evolution conditions is excellent (Fig. 11b).

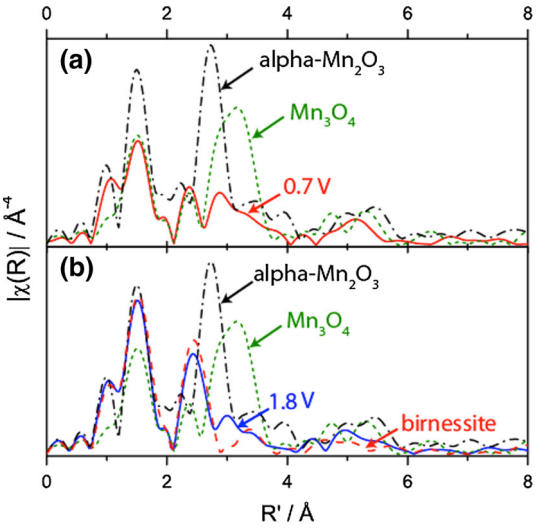

Fig. 11 EXAFS spectroscopy of Mn oxide catalytic film deposited on Au/Ti electrode under reaction conditions. **a** MnO_x/Au-Si_3N_4 film poised at 0.7 V overlaid by reference materials Mn_3O_4 and α-Mn_2O_3. **b** MnO_x/Au-Si_3O_4 film poised at 1.8 V overlaid by reference materials Mn_3O_4, α-Mn_2O_3, and birnessite. From Ref. 58, with permission

This first in situ observation of birnessite Mn oxide structure as the catalytically active phase under water oxidation conditions furnishes an important link to several recent reports of ex situ XANES measurements on other catalytically very active Mn oxide and $CaMnO_x$ preparations that reveal birnessite structure [21, 22, 60]. Surface chemical functionalities formed during the water oxidation cycle have not yet been observed for these Mn oxide catalysts, but knowledge of the structural phase during reaction is an important step towards a mechanistic understanding. The flexible layers of octahedral MnO_6 of the birnessite structure surrounded by water (Fig. 10b) offer a very large surface for catalytic Mn sites interacting with H_2O molecules.

4 Ir Oxide Catalyst: Combining Bond Specificity of Infrared Spectroscopy with Metal Electronic Structure Specificity of XPS

Ir oxide is the only known metal oxide catalyst for water oxidation that performs efficiently and stably in acid as well as base [61]. The oxide is used in commercial electrolyzers [62] and has been explored as a catalytic component in a various electrochemical cells [1, 63], photoanode assemblies [64] and integrated artificial photosystem designs [65, 66]. Large scale use of this noble metal oxide as water oxidation catalyst is prohibited by its scarcity, but mechanistic understanding will be valuable given the observed high efficiency. Direct absorption of light by IrO_2 nanoparticles (2 nm) (Ir d–d transition in the visible or O(p)−Ir(d(e.g.)) charge transfer in the UV) in the presence of an electron acceptor is capable of inducing water oxidation (though inefficiently) and has provided insights into those electronic properties of the oxide that enable water oxidation catalysis [67]. Visible light-on/off rapid-scan FT-IR monitoring in the ATR mode (light pulse of 1 s duration) of an aqueous solution of Ir nanoparticles (pH 6) in the presence of the $[Ru(bpy)_3]^{2+}$ sensitizer and persulfate electron acceptor system showed a band at 830 cm^{-1} (H_2O) that only appeared during the light-on period, as shown in Fig. 12a [68]. The same experiments in $D_2^{16}O$ and $D_2^{18}O$–$D_2^{16}O$ isotopic mixtures revealed two bands with ^{18}O shifts of 25 and 50 cm^{-1}, respectively, characteristic of ^{18}O–^{16}O and ^{18}O–^{18}O peroxide bond modes (Fig. 12b). A 30 cm^{-1} D shift in D_2O identified the intermediate as a surface hydroperoxide (IrOOH). The fact that the bands appear only during the laser pulse (1 s duration) but vanish instantly when the light is off is consistent with the known TOF of 6–10 s^{-1} for H_2O oxidation at IrO_2 [63, 69, 70] and confirms that the intermediate is a kinetically relevant species of the catalytic water oxidation cycle [68]. The observed frequency of the OO mode does not allow us to identify the metal oxidation state of the IrOOH group. Nevertheless, based on the expectation that IrOOH is formed by nucleophilic attack of H_2O on Ir^V=O, the oxidation state is likely Ir^{III}OOH (OO bond formation by nucleophilic attack of H_2O on an oxo group results in a formal 2-electron reduction of the metal). A recent ambient pressure XPS study of electrocatalytic water oxidation on IrO_2 nanoparticles under steady state conditions by Nilsson indicates the formation of Ir^V centers at catalyst surface [71]. Hence, with the direct observation of the hydroperoxide intermediate by FT-IR spectroscopy

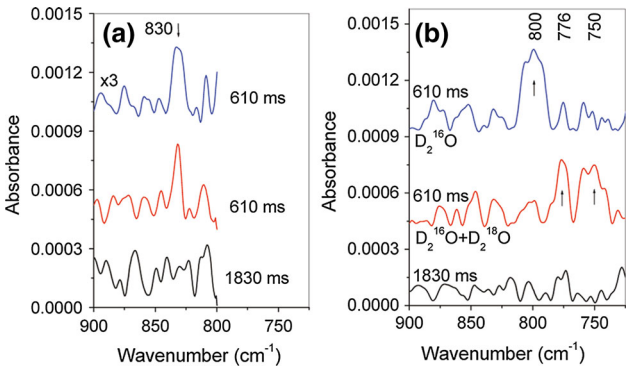

Fig. 12 Rapid-scan FT-IR spectra of IrOOH (hydroperoxide) surface intermediate of water oxidation at Ir oxide nanoparticle–aqueous solution interface. **a** 610 ms (photolysis light on) and 1,830 ms spectra (light off). **b** *Top* 610 ms time slices of experiments in $D_2^{16}O$. *Middle* $D_2^{16}O$(33 %) + $D_2^{18}O$(66 %). *Bottom* 1,830 ms time slice (light off) of experiment in $D_2^{16}O$. From Ref. 68, with permission

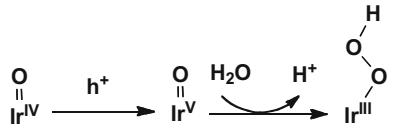

Fig. 13 Mechanism of OO bond forming step of water oxidation at Ir oxide surface. From Ref. 68, with permission

and the detection of Ir^V by XPS in aqueous media under reaction conditions, key features of the catalytic cycle begin to emerge, allowing us to propose the partial mechanism shown in Fig. 13. A surface IrOOH intermediate on $IrO_2(110)$ has been predicted by quantum chemical calculations [72]. Furthermore, an identical mechanism has been proposed for single Ir center molecular catalysts for water oxidation [73].

While the spectroscopic observations pertain only to the first (of four) charge transfer intermediates with the subsequent steps from $Ir^{III}OOH$ to O_2 still to be uncovered, these results, together with those of the Co_3O_4 study begin to establish the molecular identity of surface intermediates and detailed elementary reaction steps of water oxidation on metal oxide surfaces. Specifically, the findings confirm the dominant role of nucleophilic attack of H_2O on an electrophilic oxo metal site in O–O bond formation over a possible alternative path of direct coupling of adjacent oxo metal sites (M=O + O=M $\rightarrow$ O_2 + M + M) to liberate O_2.

5 TiO_2, $SrTiO_3$ and Fe_2O_3 Photocatalysts: Monitoring Light Induced Charge Flow Driving Chemical Transformations at the Catalyst Surface

Some metal oxides, notably TiO_2, $SrTiO_3$, Fe_2O_3 and WO_3 combine the light absorption, charge separation and catalytic function in a single crystalline material. Because of the built-in light absorption property, these systems offer the most straightforward approach for elucidating the elementary steps of charge transport across the oxide bulk to the catalyst surface and the subsequent processes that induce chemical reaction. In the case of films of TiO_2 (rutile) particles (30–50 nm) exposed to aqueous solution under UV excitation, in situ steady state FT-IR spectroscopy in the ATR mode has revealed two surface intermediates, namely TiOOH and TiOOTi [74]. Figure 14a shows the growth of the O–O stretch mode of the hydroperoxide intermediate (TiOOH) with a maximum at 838 cm^{-1} in acidic solution (pH 2.4) under continuous photolysis. Experiments were conducted as half reactions by using a sacrificial acceptor for capturing the TiO_2 conduction band electrons before they can recombine with transient valence band holes. A second surface intermediate absorbing at 812 cm^{-1} exhibits most pronounced growth over the first few minutes of photolysis and is dominant in alkaline solution (pH 11.9), as shown in Fig. 14b. It is attributed to the O–O stretch of a TiOOTi surface site. Spectral identification of both surface intermediates is supported by ^{18}O isotope labeling studies [74]. The proposed mechanism features hole transfer to a bridging O of a TiOTi surface moiety (note that hole capture by Ti^{IV} metal centers is energetically not possible) followed by nucleophilic attack of H_2O under concurrent breaking of a Ti–O bond. Coupling of adjacent Ti–O radical sites is proposed to result in the observed TiOOTi site, as shown in Fig. 15. The formation of the surface hydroperoxide intermediate in acidic solution and its absence under basic conditions is explained by partial hydrolysis of the TiOOTi group at low pH. Transfer of two additional holes liberates O_2 and restarts the photocatalytic cycle.

Using transient optical absorption spectroscopy over the entire time range from picosecond to seconds, Durrant and coworkers have monitored the behavior of holes generated upon UV excitation of TiO_2 (anatase) films. Transient holes with an absorption maximum at 460 nm with lifetimes of several seconds are detected and their kinetic behavior attributed to the rate-limiting water oxidation step of the catalytic cycle [75, 76]. Cuk and coworkers, working with single crystal *n*-$SrTiO_3$ as a highly efficient photoanode for water oxidation, combined the tuning of an applied potential with surface sensitive ultrafast optical spectroscopy to selectively monitor the charge transport processes across the surface-Helmholtz layer interface of the alkaline solution under operating conditions [77]. As shown in Fig. 16, the time dependence of the optical absorption of the photo-generated valence band hole at 800 nm indicates a process with a single rate constant that has an exponential dependence on the surface hole potential (from 3 ns to 8 ps over a 1 V potential increase). This result implies a single hole transfer step initiating water oxidation and reveals the associated activation barrier. The process, which is assigned to oxidation of hydroxide ion to OH radical and observed here as a separate process for the first time, is set apart from all subsequent hole transfers, which are much slower [77]. In light of the infrared results [74] and the mechanism proposed in Fig. 15 (and ignoring the fact that $SrTiO_3$ is used in the transient optical work), the subsequent slow process might be the formation of a $TiO(h^+)Ti$ site. These results set the stage for temporally resolved infrared monitoring under reaction conditions for uncovering the chemical identity of the surface functionality that is formed.

Transient optical spectroscopic measurements at the widely investigated Fe_2O_3 (hematite) water oxidation catalyst reveal long-lived absorptions in the 600–800 nm region (milliseconds to seconds) upon bandgap excitation,

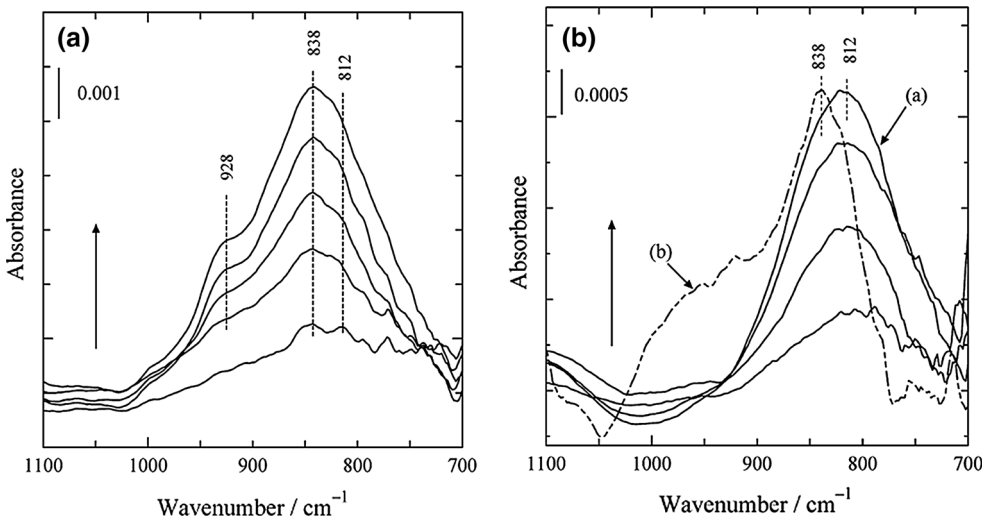

Fig. 14 FT-IR spectroscopy of TiO_2 (rutile) particles in aqueous solution under photocatalytic conditions. **a** TiO_2 film in contact with aqueous solution at pH 2.4 recorded at 1, 10, 20, 30, 40 min. After start of UV illumination. The arrow indicates the direction of the spectral change. Fe^{3+} was used as electron acceptor. **b** *Solid traces* Identical illumination protocol as in **a** but in pH 11.9 solution using loaded Pt particles as electron acceptor. *Broken trace* The Pt/TiO_2 sample was exposed to acidic (pH 2.4) conditions after UV irradiation experiment, confirming that the 812 cm^{-1} species is unique for alkaline conditions. From Ref. 74, with permission

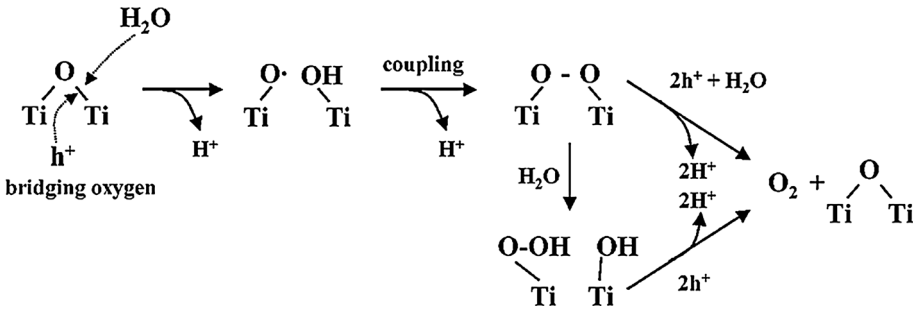

Fig. 15 Proposed reaction mechanism for photocatalytic water oxidation at TiO_2 (rutile)—aqueous interface. From Ref. 74, with permission

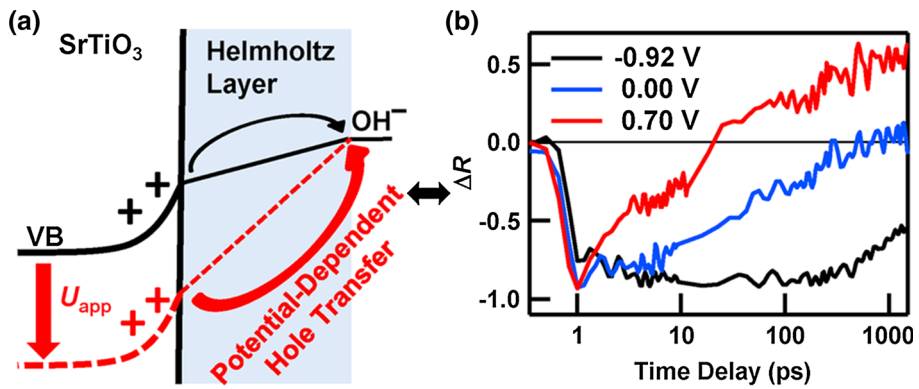

Fig. 16 Transient optical spectroscopy of hole transport across *n*-$SrTiO_3$ aqueous solution interface. **a** Schematic of processes that are probed. **b** Decay of photogenerated valence band holes probed at 800 nm as function of applied potential. From Ref. 77, with permission

which are attributed to holes involved in the catalysis [78]. Identification of the surface chemical functionality by vibrational spectroscopy is not yet available and the mechanistic meaning of the signal is currently under debate. One proposed assignment is that of a high valent Fe^{V}=O surface intermediate that subsequently would undergo electrophilic attack H_2O to yield a hydroperoxide intermediate [79]. There is convincing evidence for the same mechanism of O–O bond formation for O_2 evolving organo iron catalysts [80, 81].

Future investigations based on combined transient optical and transient vibrational spectroscopy on how

transferred charges induce catalytic transformations on the metal oxide surface need to be expanded to systems in which light absorption and catalytic function are separated. Initial systems for which hole transport from light absorber to metal oxide catalyst has already been established by transient optical measurements (observed times are milliseconds or less, in some cases ultrafast) include TiO_2–IrO_2 [82], GaN:ZnO–CoO_x [83], $[Ru(bpy)_3]^{2+}$-polyoxo-metalate ($[\{Ru_4O_4(OH)_2(H_2O)_4\}(\gamma\text{-}SiW_{10}O_{36})_2]^{10-}$) [84], and $[Ru(bpy)_3]^{2+}$–IrO_2 [85].

6 Closing the Catalytic Cycle of Water Oxidation at Metal Oxide Particle with Carbon Dioxide Reduction at Heterobinuclear Site

Water oxidation to molecular oxygen is a mandatory reaction of any photosynthetic process because it provides the electrons and protons that enable the formation of a fuel upon reaction with carbon dioxide. As an example, we discuss here the coupling O_2 evolution from water at a metal oxide catalyst with carbon dioxide reduction at an all-inorganic, oxo-bridged heterobinuclear light absorber [66].

Oxo-bridged, all-inorganic heterobinuclear units covalently anchored on a silica surface possess metal-to-metal charge-transfer (MMCT) absorptions that extend deep into the visible region. The optical absorption originates from the overlap of the d orbitals of the two metal centers. Units with appropriate redox potentials are capable of driving a water oxidation catalyst, others reduce CO_2 to CO or formate. Todate, a dozen different systems featuring Ti or Zr as acceptor and a first or second row transition metal as donor center have been developed [86–97]. The detailed structure of several units on the surface of mesoporous silica supports, including the $ZrOCo^{II}$ system shown in Fig. 17a has been determined by EXAFS spectroscopy [66, 96, 97]. Typical metal-to-metal distances are around 3.4 A. The optical MMCT absorption $Zr^{IV}OCo^{II} \rightarrow Zr^{III}OCo^{III}$, shown in Fig. 17b, extends from the UV into the visible region with an onset around 550 nm. The ability of most binuclear units to drive MMCT induced redox reactions is attributed to an unusually long lifetime of the excited charge transfer state which has its origin in ultrafast spin crossover after light absorption that results in slow back electron transfer. In the case of the $TiOMn^{II}$ system, the lifetime was determined as 2.4 μs at room temperature by transient optical absorption spectroscopy [95, 98].

In an attempt to couple a metal oxide nanocatalyst for water oxidation with a heterobinuclear MMCT unit for accomplishing CO_2 reduction by electrons donated by H_2O, we have developed a photodeposition method for coupling a binuclear light absorber to an Ir oxide nanocluster. The $ZrOCo^{II}$ unit was selected because it was found to reduce vapor phase CO_2 to CO and formate upon visible or UV excitation of the charge transfer state in the presence of triethylamine as a sacrificial donor [97]. Since transient Co^{III} center generated upon excitation of the MMCT state has an oxidation potential around +1.8 V, it should be possible to simultaneously drive a water oxidation catalyst with this unit. Development of a photodeposition method for proper positioning of an Ir oxide nanocluster catalyst adjacent to the Co donor center of a ZrOCo unit in the channels of mesoporous silica SBA-15 allowed us to synthesize polynuclear units consisting of a ZrOCo charge-transfer chromophore coupled to an IrO_x nanocluster catalyst. The spatially directed assembly of the Ir oxide clusters was monitored by optical and FT-IR spectroscopy, and their size of the 2 nm established by HAADF-STEM imaging and EDX measurements [66].

When illuminating the MMCT absorption of $ZrOCo^{II}$–IrO_x units supported on SBA-15 loaded with a gas mixture

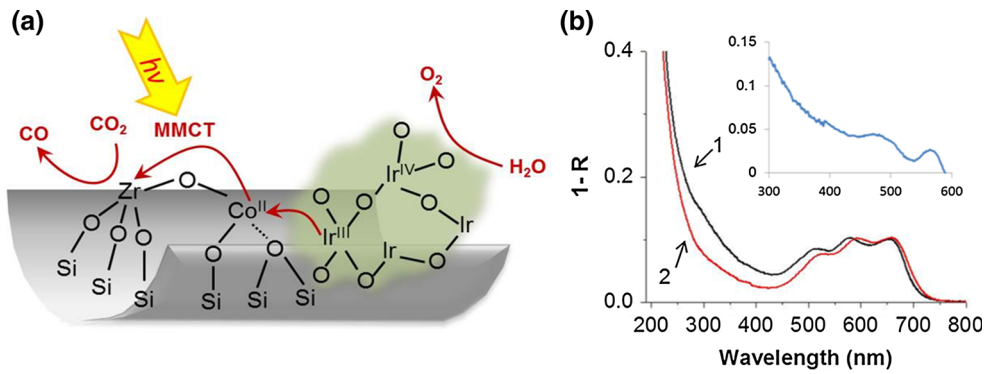

Fig. 17 Photosynthetic unit for CO_2 reduction by H_2O consisting of a binuclear $ZrOCo^{II}$ charge-transfer light absorber coupled to a 2 nm Ir oxide nanocluster catalyst. **a** Schematic of assembly. **b** UV–Vis diffuse reflectance spectra of $ZrOCo^{II}$ unit anchored in the channels of mesoporous silica SBA-15 (*black trace* 1). The *red trace* (2) shows the spectrum of isolated Co^{II} centers anchored on SBA-15. *Inset* Difference spectrum $ZrOCo^{II}$ minus Co^{II} sample showing the metal-to-metal charge-transfer absorption. From Ref. 97, with permission

of $^{13}CO_2$ and H_2O with 355 nm light, growth of ^{13}CO and O_2 product was observed by in situ FT-IR spectroscopy and mass spectrometry, respectively. As shown in Fig. 18a, gas phase ^{13}CO product grew in linearly (a partial ro-vibrational spectrum is presented). The CO is formed inside the 8 nm diameter silica channels and desorbs into the gas phase with a 340 μs escape time according to a previous transient FT-IR study [99]. Oxygen gas is detected mass spectrometrically (Fig. 18b). When conducting the photochemical experiment with a mixture of $^{13}C^{16}O_2$ and $H_2^{18}O$, isotopically labeled $^{18}O_2$ was detected as well (Fig. 18c), establishing water as the electron source for CO_2 reduction. No CO or O_2 product appeared when omitting H_2O, which further confirmed that water serves as electron source. Also, no CO or O_2 was produced when conducting photolysis in the presence of all components but omitting the photo-deposition procedure for preparing the IrO_x clusters. Hence, photodepositon is a required step for establishing charge transfer coupling between the Co donor of the light absorber and the Ir oxide catalyst. The observed conversion of CO_2 to CO and O_2 ($\Delta G° = 62$ kcal mol^{-1}) with H_2O as electron source under illumination with 355 nm photons is consistent with the energetics of the reaction and in agreement with our previous results on the corresponding oxidation and reduction half reactions [66]. The quantum efficiency is estimated at 17 % assuming that there is no energy transfer between individual photocatalytic sites. This is the first observation of CO_2 photoreduction by H_2O at an all-inorganic polynuclear light absorber-catalyst assembly with a molecularly defined chromophore. The system shows that direct coupling of a metal oxide catalyst for water oxidation with an inorganic charge transfer chromophore for CO_2 reduction is feasible, and opens up detailed exploration of elementary charge transfer and catalytic steps of the complete cycle with vibrational, optical and X-ray techniques.

7 Conclusions

The discovery of new nanostructured forms of first row transition metal oxides in the past several years, foremost of Co and Mn that function as remarkably active water oxidation catalysts has attracted the attention of a number of catalysis groups to the challenge of elucidating the step-by-step mechanisms of the four-electron transfer chemistry at the aqueous solution-solid interface. For Co_3O_4, bond modes of a superoxo and an oxo Co^{IV} species were detected by infrared spectroscopy, with the role of the surface intermediates in the catalytic cycle identified by their temporal behavior under reaction conditions. Ex situ EPR measurements of Co oxide electrodeposits revealed the formation of Co^{IV} surface species, and steady-state

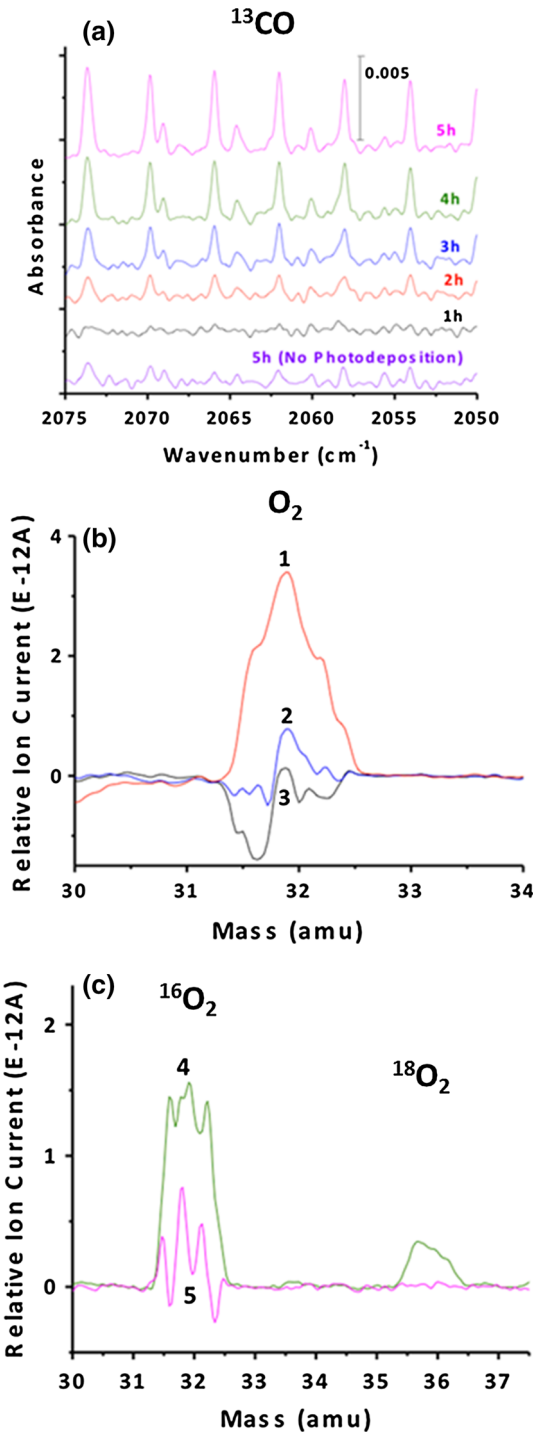

Fig. 18 Spectroscopy of photoreduction of CO_2 by H_2O at $ZrOCo^{II}$–IrO_x unit anchored in SBA-15. **a** Growth of infrared bands of gas phase ^{13}CO upon illumination (355 nm) of the MMCT absorption in the presence of a gaseous mixture of $^{13}CO_2$ and H_2O. The *bottom trace* shows that no product growth is observed upon illumination if the Ir oxide nanocluster is synthesized without the photodeposition procedure. **b** *Trace 1* Detection of O_2 product by mass spectroscopy. No O_2 is formed in the absence of H_2O (*trace 2*) or without illumination (*trace 3*) for otherwise identical samples. **c** Mass spectra of $^{18}O_2$ and $^{16}O_2$ produced under identical experimental conditions using $^{13}CO_2$ and $H_2^{18}O$ (*trace 4*). *Trace 5* shows control in the absence of illumination. From Ref. 66, with permission

in situ X-ray spectroscopy confirmed that the oxidation state of Co rises above III under electrocatalytic oxygen evolution. In situ monitoring of XANES spectra for identifying structural phases present under electrocatalytic conditions has been particularly insightful in the case of Mn oxide catalysts. Rapid-scan FT-IR measurements and ambient pressure XPS results of Ir oxide water oxidation catalysts illustrate the need to probe bond modes and metal electronic structure with these complementary techniques in order to understand the chemical functionalities formed in the catalytic cycle.

When combined with temporally resolved optical monitoring of charge delivery to the catalytic surface site as demonstrated in the case of Fe_2O_3 or $SrTiO_3$ photocatalysts, future experiments will explore the detection, by vibrational spectroscopy, of molecular surface intermediates formed by specific charge injection events along the catalytic cycle. Such measurements are the key for pinpointing kinetic bottlenecks and provide the information needed for redesigning surface sites to improve efficiency. Furthermore, by combining temporally resolved infrared spectroscopy of surface intermediates with monitoring of the electronic structure of the metal oxide surface using ultrafast hard and soft X-ray free electron laser sources will greatly enhance our understanding of these multi-electron catalytic processes. The recent demonstration of time-resolved X-ray emission spectroscopy for elucidating the O_2-forming step of Nature's water oxidation cycle at the $CaMn_4O_4$ cluster of Photosystem II provides an inspiring example of the use of the emerging ultrafast X-ray free electron laser techniques [100]. Such efforts will play a key role in accelerating progress towards efficient metal oxide catalysts for water oxidation, and the coupling to carbon dioxide reduction.

Acknowledgments This material is based on work supported by the U.S. Department of Energy, Office of Science, Office of Basic Energy Sciences under contract No. DE-AC02-05CH11231. This research used resources of the National Center for Electron Microscopy, Lawrence Berkeley National Laboratory, which is a DOE Office of Science User Facility. The authors thank Dr. Christian Kisielowski for imaging at the TEAM0.5 microscope.

References

1. Trasatti S (1984) Electrochim Acta 29:1503
2. El-Deab MS, Awad MI, Mohammad AM, Ohsaka T (2007) Electrochem Commun 9:2082
3. Matsumoto Y, Sato E (1986) Mater Chem Phys 14:397
4. Iwakura C, Honji A, Tamura H (1981) Electrochim Acta 26:1319
5. Rasiyah P, Tseung ACC (1983) J Electrochem Soc 130:365
6. Singh RN, Mishra D, Anindita M, Shinha ASK, Singh A (2007) Electrochem Commun 9:1369
7. Schmidt T, Wendt H (1994) Electrochim Acta 39:1763
8. Morita M, Iwakura C, Tamura H (1978) Electrochim Acta 23:331
9. Morita M, Iwakura C, Tamura H (1979) Electrochim Acta 24:357
10. Mraz R, Srb V, Tichy S (1973) Electrochim Acta 18:551
11. Matsumoto Y, Sato E (1979) Electrochim Acta 24:421
12. Fujimura K, Matsui T, Izumiya K, Kumagai N, Akiyama E, Habazaki H, Kawashima K, Asami K, Hashimoto K (1999) Mater Sci Eng, A 267:254
13. Morita M, Iwakura C, Tamaru H (1977) Electrochim Acta 22:325
14. Okuno Y, Yonemitsu O, Chiba Y (1983) Chem Lett 12:815
15. Shafirovich VY, Khannanov NK, Shilov AE (1981) J Inorg Biochem 15:113
16. Harriman A, Pickering IJ, Thomas JM, Christensen PA (1988) J Chem Soc, Faraday Trans I(84):2795
17. Jiao F, Frei H (2009) Angew Chem Int Ed 48:1841
18. Jiao F, Frei H (2010) Energy Environ Sci 3:1018
19. Jiao F, Frei H (2010) Chem Commun 46:2920
20. Pushkar Y, Yano J, Sauer K, Boussac A, Yachandra VK (2008) Proc Natl Acad Sci USA 105:1879
21. Zaharieva I, Najafpour MM, Wiechen M, Haumann M, Kurz P, Dau H (2011) Energy Environ Sci 4:2400
22. Wiechen M, Zaharieva I, Dau H, Kurz P (2012) Chem Sci 3:2330
23. Frey CE, Wiechen M, Kurz P (2014) Dalton Trans 43:4370
24. Gardner GP, Go YB, Robinson DM, Smith PF, Hadermann J, Abakumov A, Greenblatt M, Dismukes GC (2012) Angew Chem Int Ed 51:1616
25. Hara M, Lean JT, Mallouk TE (2001) Chem Mater 13:4668
26. Grzelczak M, Zhang J, Pfrommer J, Hartmann J, Driess M, Antonietti M, Wang X (2013) ACS Catal 3:383
27. Yusuf S, Jiao F (2012) ACS Catal 2:2753
28. Esswein AJ, McMurdo MJ, Ross PN, Bell AT, Tilley TD (2009) J Phys Chem C 113:15068
29. Soo HS, Agiral A, Bachmeier A, Frei H (2012) J Am Chem Soc 134:17104
30. Agiral A, Soo HS, Frei H (2013) Chem Mater 25:2264
31. Yuan G, Agiral A, Pellet N, Kim W, Frei H (2014) Faraday Disc. doi:10.1039/C4FD00150H
32. Zhang M, de Respinis M, Frei H (2014) Nat Chem 6:362
33. Kisielowski C, Helveg S, Yuan G, Frei H (2014) Micron. doi:10.1016/j.micron.2014.07.009
34. Zecchina A, Spoto G, Coluccia S (1982) J Mol Catal 14:351
35. McAlpin JG, Surendranath Y, Dinca M, Stich TA, Stoian SA, Casey WH, Nocera DG, Britt RD (2010) J Am Chem Soc 132:6882
36. Gerken JB, McAlpin JG, Chen JYC, Rigsby ML, Casey WH, Britt RD, Stahl SS (2011) J Am Chem Soc 133:14431
37. Xu XL, Chen ZH, Li Y, Chen WK, Li JQ (2009) Surf Sci 603:653
38. Kanan MW, Nocera DG (2008) Science 231:1072
39. Surendranath Y, Kanan MW, Nocera DG (2010) J Am Chem Soc 132:16501
40. Kanan MW, Yano J, Surendranath Y, Dinca M, Yachandra VK, Nocera DG (2010) J Am Chem Soc 132:13692
41. McAlpin JG, Stich TA, Ohlin CA, Surendranath Y, Nocera DG, Casey WH, Britt RD (2011) J Am Chem Soc 133:15444
42. Du P, Kokhan O, Chapman KW, Chupas PJ, Tiede DM (2012) J Am Chem Soc 134:11096
43. Mulfort KL, Mukherjee A, Kokhan O, Du P, Tiede DM (2013) Chem Soc Rev 42:2215
44. Chivot J, Mendoza L, Mansour C, Pauporte T, Cassir M (2008) Corros Sci 50:62
45. Yeo BS, Bell AT (2011) J Am Chem Soc 133:5587
46. Subbaraman R, Tripkovic D, Chang KC, Strmcnik D, Paulikas AP, Hirunsit P, Chan M, Greeley J, Stamenkovic D, Markovic NM (2012) Nat Mater 11:550

47. Garcia-Mota M, Bajdich M, Viswanathan V, Vojvodic A, Bell AT, Norskov JK (2012) J Phys Chem C 116:21077
48. Bajdich M, Garcia-Mota M, Vojvodic A, Norskov JK, Bell AT (2013) J Am Chem Soc 135:13521
49. Yin Q, Tan JM, Besson C, Geletti YV, Musaev DG, Kuznetsov AE, Luo Z, Hardcastle KI, Hill CL (2010) Science 328:341
50. Liu F, Concepcion JJ, Jurss JW, Cardolaccia T, Templeton JL, Meyer TJ (2008) Inorg Chem 47:1727
51. Concepcion JJ, Jurss JW, Templeton JL, Meyer TJ (2008) Proc Natl Acad Sci 105:17632
52. Tseng HW, Zong R, Muckerman JT, Thummel RP (2008) Inorg Chem 47:11763
53. Concepcion JJ, Jurss JW, Templeton JL, Meyer TJ (2008) J Am Chem Soc 130:16462
54. Polyansky DE, Muckerman JT, Rochford J, Zong R, Thummel RP, Fujita E (2011) J Am Chem Soc 133:14649
55. Wasylenko DJ, Palmer RD, Berlinguette CP (2013) Chem Commun 49:218
56. Boppana VBR, Jiao F (2011) Chem Commun 47:8973
57. Takashima T, Hashimoto K, Nakamura R (2012) J Am Chem Soc 134:1519
58. Gorlin Y, Lassalle-Kaiser B, Benck JD, Gul S, Webb SM, Yachandra VK, Yano J, Jaramillo TF (2013) J Am Chem Soc 135:8525
59. Gorlin Y, Jaramillo TF (2010) J Am Chem Soc 132:13612
60. Hocking RK, Brimblecombe R, Chang LY, Singh A, Cheah MH, Clover C, Casey WH, Speccia L (2011) Nat Chem 3:461
61. McCrory C, Jung S, Peters JC, Jaramillo TF (2013) J Am Chem Soc 135:16977
62. Tilak BV (1981) In: Bockris JOM (eds) Comprehensive Treatise of Electrochemistry, vol. 2. Plenum Press: New York, p 1
63. Nakagawa T, Bjorge NS, Murray RW (2009) J Am Chem Soc 131:15578
64. Spurgeon JM, Velasquez JM, McDowell MT (2014) PhysChemChemPhys 16:3623
65. Swierk JR, Mallouk TE (2013) Chem Soc Rev 42:2357
66. Kim W, Yuan G, McClure BA, Frei H (2014) J Am Chem Soc 136:11034
67. Frame FA, Townsend TK, Chamousis RL, Sabio EM, Dittrich T, Browning ND, Osterloh FE (2011) J Am Chem Soc 133:7264
68. Sivasankar N, Weare WW, Frei H (2011) J Am Chem Soc 133:12976
69. Nagakawa T, Beasley CA, Murray RW (2009) J Phys Chem C 113:12958
70. Kuwabara T, Tomita E, Sakita S, Hasegawa D, Sone K, Yagi M (2008) J Phys Chem C 112:3774
71. Sanchez Casalongue HG, Ng ML, Kaya S, Friebel D, Ogasawara H, Nilsson A (2014) Angew Chem Int Ed 53:7169
72. Rossmeisl J, Qu ZW, Zhu H, Kroes GJ, Norskov JK (2007) J Electroanal Chem 607:83
73. Blakemore JD, Schley ND, Balcells D, Hull JF, Olack GW, Incarvito CD, Eisenstein O, Brudvig GW, Crabtree RH (2010) J Am Chem Soc 132:16017
74. Nakamura R, Nakato Y (2004) J Am Chem Soc 126:1290
75. Cowan AJ, Tang J, Leng W, Durrant JR, Klug DR (2010) J Phys Chem C 114:4208
76. Cowan AJ, Barnett CJ, Pendlebury SR, Barroso M, Sivula K, Graetzel M, Durrant JR, Klug DR (2011) J Am Chem Soc 133:10134
77. Waegele MM, Chen X, Herlihy DM, Cuk T (2014) J Am Chem Soc 136:10632
78. Barroso M, Mesa CA, Pendlebury SR, Cowan AJ, Hisatomi T, Sivula K, Graetzel M, Klug DR, Durrant JR (2012) Proc Natl Acad Sci USA 109:15640
79. Young KMH, Klahr BM, Zandi O, Hamann TW (2013) Catal Sci Technol 3:1660
80. Chadwick Ellis W, McDaniel ND, Bernhard S, Collins TJ (2010) J Am Chem Soc 132:10990
81. Fillol JL, Codola Z, Garcia-Bosch I, Gomez L, Pla JJ, Costas M (2011) Nat Chem 3:807
82. Meekins BH, Kamat PV (2011) J Phys Chem Lett 2:2304
83. Yamakata A, Kawaguchi M, Nishimura N, Minegishi T, Kubota J, Domen K (2014) J Phys Chem C 118:23897
84. Xiang X, Fielden J, Rodriguez-Cordoba W, Huang Z, Zhang N, Luo Z, Musaev DG, Lian T, Hill CL (2013) J Phys Chem C 117:918
85. Youngblood WJ, Lee SHA, Kobayashi Y, Hernandez-Pagan EA, Hoertz PG, Moore TA, Moore AL, Gust D, Mallouk TE (2009) J Am Chem Soc 131:926
86. Lin W, Frei H (2005) J Am Chem Soc 127:1610
87. Lin W, Frei H (2005) J Phys Chem B 109:4929
88. Han H, Frei H (2007) Microporous Mesoporous Mater 103:265
89. Han H, Frei H (2008) J Phys Chem C 112:8391
90. Han H, Frei H (2008) J Phys Chem C 112:16156
91. Okamoto A, Nakamura R, Osawa H, Hashimoto K (2008) Langmuir 24:7011
92. Okamoto A, Nakamura R, Osawa H, Hashimoto K (2008) J Phys Chem C 112:19777
93. Wu X, Weare WW, Frei H (2008) Dalton Trans: 10114
94. Frei H (2009) Chimia 63:721
95. Cuk T, Weare WW, Frei H (2010) J Phys Chem C 114:9167
96. Soo HS, Macnaughtan ML, Weare WW, Yano J, Frei H (2011) J Phys Chem C 115:24893
97. Macnaughtan ML, Soo HS, Frei H (2014) J Phys Chem C 118:7874
98. McClure BA, Frei H (2014) J Phys Chem C 118:11601
99. Andersen LK, Frei H (2006) J Phys Chem B 110:22601
100. Kern J et al (2014) Nat Commun. doi:10.1038/ncomms5371